

Energy & Environmental Science

rsc.li/ees



ISSN 1754-5706



Cite this: *Energy Environ. Sci.*, 2021, 14, 5347

Sustainable off-grid desalination of hypersaline waters using Janus wood evaporators[†]

Xi Chen, ^a Shuaiming He, ^b Mark M. Falinski, ^a Yuxi Wang, ^{ac} Tian Li, ^b Sunxiang Zheng, ^a Dongya Sun, ^a Jiaqi Dai, ^b Yanhong Bian, ^a Xiaobo Zhu, ^a Jinyue Jiang, ^a Liangbing Hu ^{*b} and Zhiyong Jason Ren ^{*a}

Solar-thermal evaporation is a promising technology for energy-efficient desalination, but salt accumulation on solar absorbers and system longevity are the major challenges that hinder its widespread application. In this study, we present a sustainable Janus wood evaporator that overcomes these challenges and achieves a record-high evaporation efficiencies in hypersaline water, one of the most difficult water sources to treat via desalination. The Janus wood evaporator has asymmetric surface wettability, where the top layer acts as a hydrophobic solar absorber with water blockage and salt resistance, while the bottom hydrophilic wood layer allows for rapid water replenishment and superior thermal insulation. An evaporation efficiency of 82.0% is achieved for 20% NaCl solution under 1 sun, and persistent salt-resistance is observed during a 10-cycle long-term test. To ensure the environmental impact of the Janus wood evaporator, for the first time, a life cycle assessment (LCA) is conducted to compare this Janus wood evaporator with the emerging Janus evaporators, indicating a functional and more sustainable opportunity for off-grid desalination and humanitarian efforts.

Received 18th May 2021,
Accepted 20th July 2021

DOI: 10.1039/d1ee01505b

rsc.li/ees

Broader context

Desalination of hypersaline water is among the most difficult challenges in water management due to its high energy demand, concentrate disposal, and high cost. Solar-thermal desalination utilizes renewable energy and reduces carbon footprint, but few studies addressed the pressing issues on salt accumulation, performance degradation, and material sustainability. In this study, we report a first Janus wood evaporator with asymmetric wettability that achieved record-high evaporation efficiencies in hypersaline water without liquid discharge or salt accumulation. We also quantified the sustainability measures on different solar evaporators and found that the CO₂e emission by Janus wood evaporators could be two orders of magnitude lower than those by other types.

Introduction

The growing threats of global freshwater scarcity and climate change are driving an increased reliance on unconventional water sources such as seawater or brackish groundwater.^{1–3} As a result, water desalination capacity has more than tripled over the past 20 years.⁴ Reverse osmosis (RO) is the existing benchmark process due to its relatively low electricity consumption.⁵ However, the energy demand in the RO process greatly increases when desalinating hypersaline water because

a higher pressure is required to overcome the increased osmosis pressure.^{6,7} This hinders the potential application of RO for treating high-salinity waters, while also resulting in incomplete extraction of fresh water and generation of a concentrated brine.^{8–10} Therefore, novel processes that can achieve low-energy desalination, particularly for hypersaline waters, become essential to make desalination sustainable and affordable. Photovoltaic-powered RO processes (PV-RO) provided a new approach for off-grid water desalination,¹¹ and the recent PV performance improvement greatly facilitated PV-RO development.^{12,13} PV-RO requires the affiliation with PV panels, which take additional investment, and the treatment of hypersaline water is still challenging. In this context, the emerging solar-thermal evaporation processes carry strong promise, as they take advantage of the abundant and low-cost solar energy to achieve off-grid desalination and have the potential to reach the goal of zero liquid discharge (ZLD).^{14–17}

^a Department of Civil and Environmental Engineering and Andlinger Center for Energy and the Environment, Princeton University, Princeton, NJ 08544, USA. E-mail: zjren@princeton.edu

^b Department of Materials Science and Engineering, University of Maryland, College Park, MD 20742, USA. E-mail: binghu@umd.edu

^c The Earth Institute and School of International and Public Affairs, Columbia University, New York, NY 10027, USA

† Electronic supplementary information (ESI) available. See DOI: 10.1039/d1ee01505b

Solar-thermal evaporation is a facile process that does not require electricity infrastructure and can be modularized for easy deployment.^{18–20} Modern solar evaporators achieve enhanced evaporation efficiency by enhancing light absorption and minimizing heat losses,^{21–25} but salt accumulation and system longevity are still major challenges that hinder their widespread adoption.^{26–29} During solar-thermal evaporation, the salt concentration continuously increases on the photo-thermal material surface, leading to crystallization, which can result in severe performance drop due to the physical blocking of solar absorption sites, which subsequently decreases steam generation.^{30–32} Attempts have been made to solve this problem by using nanomaterial-based Janus thin-film evaporators with asymmetric surface wettability, and the results have shown that desalination performance remained stable without severe salt accumulation under low-salinity conditions (~3.5 wt%).^{33,34} However, there is a great need for systems that can handle hypersaline brines of 20–25 wt%. Furthermore, these Janus thin-film evaporators, with a thickness of <1 mm, had inferior thermal insulation and evaporation efficiency (Table S1, ESI†). To achieve better performance, thicker Janus evaporators would need to be utilized. However, this would likely increase the cost and complexity of fabrication, as well as the environmental impact of the whole system.

While a high level of performance is essential, there is also concern about the environmental impact of the evaporator material. The majority of current solar evaporators are made of petroleum-based products or nanomaterials, which have a considerably high carbon footprint and carry a high cost, which prevent their use in large-scale applications. Therefore, more sustainable materials like natural wood can instead serve as alternative evaporator materials for more sustainable solar steam generation. However, natural wood evaporators suffer from severe salt-accumulation and a corresponding performance decay, and the only way to achieve salt-rejection was based on the alternative salt pathways through large holes which leads to unsatisfactory heat localization and a low evaporation efficiency (57%).³⁵

In this study, we present a novel Janus wood evaporator with asymmetric wettability for solar-thermal evaporation that guaranteed great salt-resistance, thermal insulation, and evaporation efficiency toward hypersaline water desalination (Fig. 1A). Among all the reported Janus evaporators with salt resistance, the newly engineered Janus wood evaporator achieved the highest evaporation efficiency and maintained stable performance in the highest salinity (20 wt%) brines, while proving to be the most sustainable evaporative system (Fig. 1B). Additionally, for the first time, a life cycle assessment (LCA) for solar evaporation systems was developed which compared the Janus wood with other emerging Janus evaporators and high-pressure desalination systems to evaluate each system's relative embodied carbon during the extraction, manufacturing, and use phases (Fig. 1C). Taking into consideration the facile fabrication, wide availability of wood materials, low cost, stable performance, and relatively low global warming potential, Janus wood evaporators have the potential to be a solution for sustainable water desalination and ZLD.

Results and discussion

Principles of a Janus wood evaporator

Water and salt crystals reflect solar irradiation that leads to reduced efficiency, and, as a result, the solar absorber surface needs to be kept dry and clean to maintain high solar absorption. However, for traditional solar evaporators with uniform hydrophilic structures, saline water is directly lifted onto the evaporator surface, where the water quickly evaporates, leaving behind salt deposits, which could hinder solar-absorption and block evaporation (Fig. 1C). To decouple the evaporative process from the solar absorption surface and prevent salt accumulation, the Janus wood evaporator employs a thin hydrophobic solar absorber surface layer with a thick hydrophilic wood substrate bottom layer (Fig. 1A). Saline water is lifted upward by capillary forces through the hydrophilic mesoporous wood structure, stopping at the hydrophilic–hydrophobic Janus interface. In doing so, the water–air interface is relocated inside the evaporator instead of on the top layer. Despite the increase in the local salt concentration at this water–air interface during water evaporation, the salt ions can freely diffuse back to the water reservoir, rather than forming solid crystals, since the large pore sizes in the wood structure had little effects on ion diffusivity (details in the next section). Meanwhile, the hydrophobic top layer improves heat localization and reduces heat loss, allowing the surface temperature of the Janus wood evaporator to be higher than that of a uniform natural wood evaporator (Fig. S1 and S2, ESI†). As a result, a Janus wood evaporator has the potential for higher-efficiency solar desalination/ZLD with improved salt-resistance than previously reported more uniform evaporators.

Janus wood evaporator design

Two common tree species, basswood and balsawood, were tested as potential Janus wood evaporators. For each sample, natural wood was cut longitudinally and radially and then treated with surface carbonization (Fig. S3–S5, ESI†). Then, the surface temperature and solar-thermal evaporation performance were tested under the same conditions (Fig. S6 and S7, ESI†). Basswood with parallel cutting showed the best overall performance (details in Note 1, ESI†) and was therefore used in the subsequent studies.

Fig. 2 shows the morphology and physical characterization of the Janus wood evaporator. After being functionalized by perfluorodecyltriethoxysilane (FAS) to improve hydrophobicity, the top surface of the Janus wood rejected liquid water penetration and had a large contact angle of 141° (Fig. 2B), while the untreated surface control sample remained highly hydrophilic with a contact angle of 32° (Fig. S8, ESI†). The contact angle of the Janus wood surface was among the highest compared to more expensive nanoparticle-based hydrophobic layers commonly found in Janus film evaporators, including carbon black nanoparticles coated with polymethylmethacrylate (PMMA), gold nanorods (AuNR), and Ti₃C₂ nanosheets.^{33,34,36} The superior hydrophobicity of the Janus wood surface was attributed to the FAS treatment, which has a very low surface energy of

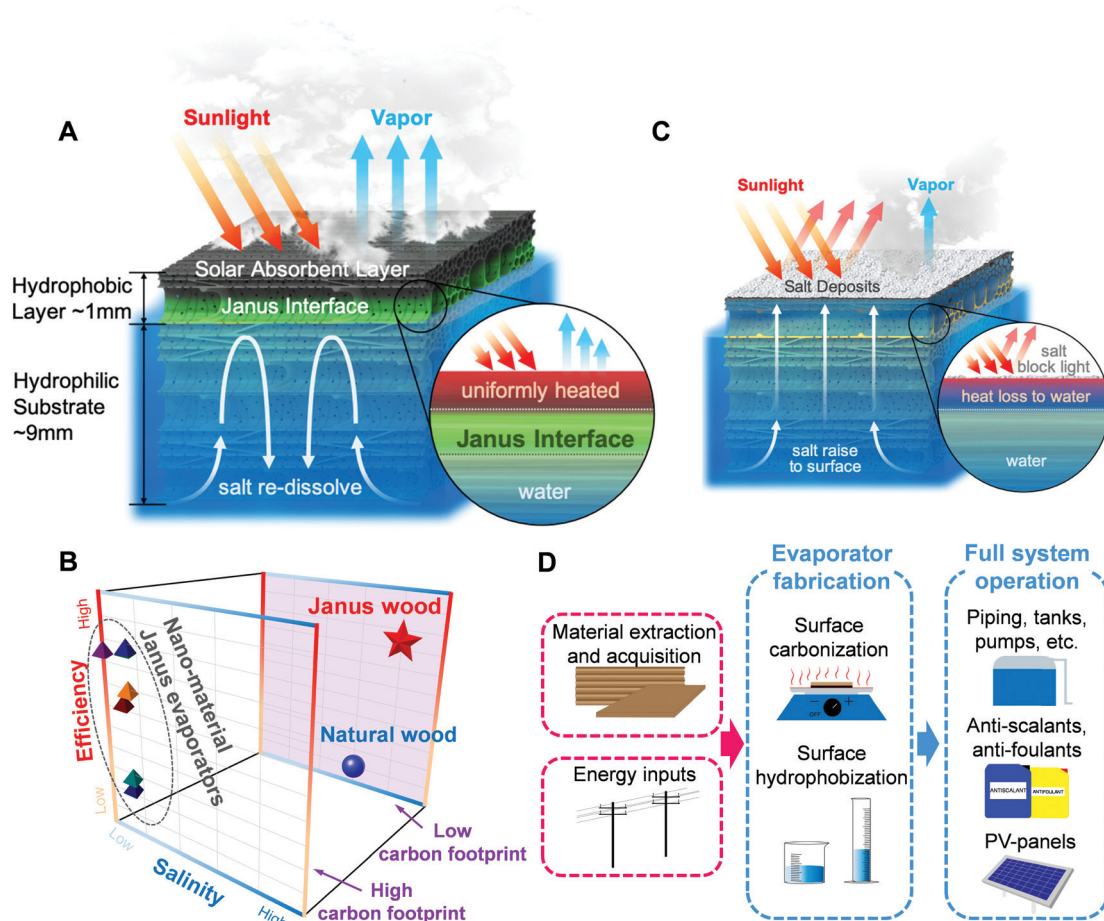


Fig. 1 Janus wood as a salt-resistant and sustainable evaporator. (A) Schematic of a Janus wood evaporator for solar-thermal evaporation, where the Janus interface enhanced the thermal insulation and improved the performance. (B) Performance comparison of the Janus wood evaporator, the natural wood evaporator and the nanomaterial-based Janus thin-film evaporators. The front panel represents a high level of carbon footprint, and the back panel represents a low level of carbon footprint. Note that only the studies that claimed salt resistance were included in this comparison. (C) Salt accumulation caused severe performance decay in a natural wood evaporator. (D) Scope of the life cycle assessment for the Janus wood evaporator system for hypersaline water desalination.

13.1 mN m⁻¹ and is highly effective in modifying the abundant -OH groups on the cellulose in wood (Fig. S9, ESI[†]). In contrast to the top surface, the bottom surface of the Janus wood remained highly hydrophilic (contact angle of 28°) and was quickly wetted by water (Fig. 2C). The contrasting chemical properties on each side of the Janus wood guaranteed fast saline water transport from the bottom *via* capillary forces, while inhibiting salt accumulation on the top solar absorber layer.

In addition, the unique hierarchical mesoporous structure of Janus wood enabled fast mass transport and excellent heat localization and insulation. Scanning electron microscopy (SEM) images show an abundance of channels aligned horizontally in the Janus wood (Fig. 2D). These channels are tree vessels (~ 50 μm in diameter) and tracheids (~ 10 μm in diameter) that form along the growth direction,³⁷ which were well-preserved from the wood block after carbonization and hydrophobization. These channels are aligned parallelly (Fig. 2E) and interconnected *via* small pores called pits ($1\text{--}2$ μm in diameter), which are distributed along the vessel

walls (Fig. 2F and G). The channels and pits form a 3-dimensional mass transfer network inside the wood. The big channels facilitate ion diffusion in the horizontal direction and help equalize saline water concentration to prevent local salinity build-up. Meanwhile, the small pits on vessel walls allow fast ion diffusion in the vertical direction (the detailed calculation of ion diffusivity in the wood structure is presented in Note 2, ESI[†]). Moreover, the anisotropic structure of Janus wood provides a very low thermal conductivity of ~ 0.11 W m⁻¹ K⁻¹, which increases thermal insulation and heat localization in the vertical direction and enables higher-efficiency solar-driven evaporation.³⁸

Record-high performance with concentrated brine

The photothermal conversion performance was tested using an optical solar incidence of 3 suns, and the surface temperature difference between the Janus wood evaporator and a natural wood evaporator without FAS treatment was compared. The results showed that the surface temperature of the natural

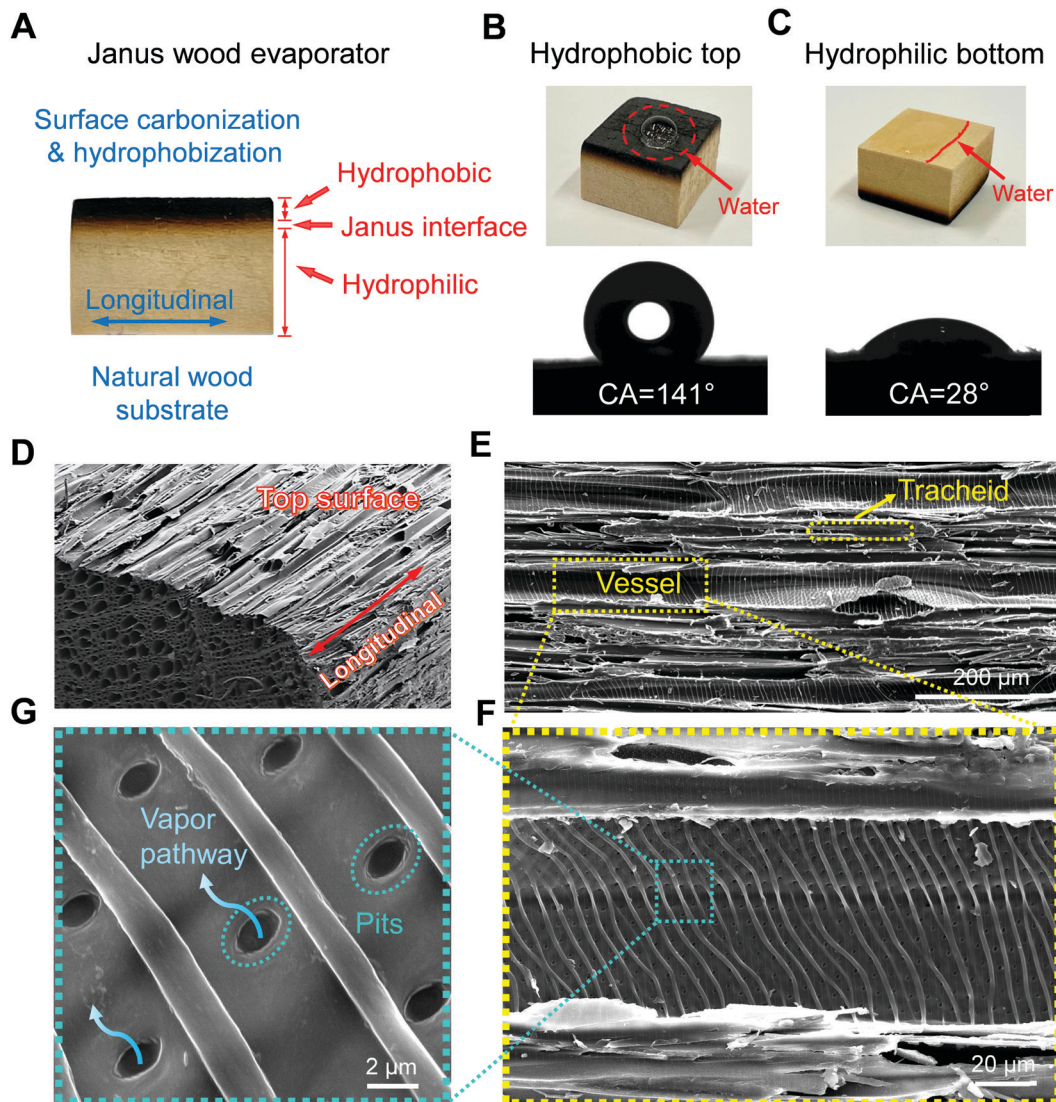


Fig. 2 Characterization showing the asymmetric wettability and the hierarchical porous structure of the Janus wood evaporator. (A) The digital image of a Janus wood evaporator. (B) The top surface was modified into hydrophobic with a large contact angle (CA) and rejected water penetration. (C) The bottom layer maintained the hydrophilic nature of wood and was quickly wetted by water drops. (D) SEM image showing the hierarchical structure of Janus wood. (E) Magnified SEM image showing aligned vessels and tracheids on the top surface. (F) Magnified SEM image showing the vessel wall structure. (G) Magnified SEM images showing the abundantly distributed pits on the vessel wall.

wood control increased from 22.4 °C to 47.2 °C after 1 min. Meanwhile, the surface temperature of Janus wood increased from 22.2 °C to 56.1 °C within 1 min (Fig. 3A). The stable surface temperature of the Janus wood evaporator under 3 suns could reach 64.7 °C after 15 min, while the bulk brine temperature remained below 29 °C (Fig. 3B). In contrast, the natural wood evaporator reached a lower surface temperature of 57.5 °C after 15 min, while the bulk brine reached a higher temperature (30.5 °C).

COMSOL was used to simulate the temperature distribution and heat transfer in Janus/natural wood solar-thermal evaporation systems. The hydrophobic top layer filled with air/vapor has a low thermal conductivity of $\sim 0.1 \text{ W m}^{-1} \text{ K}^{-1}$, which enhanced heat insulation and localization in the Janus wood

evaporator (Fig. 3C) and supported a large temperature gradient of 35.7 °C. In contrast, the top layer of the natural wood evaporator was filled with water with inferior heat insulation (Fig. S1B, ESI†). Fig. 3D shows the high temperature gradient between the top and bottom layers of the Janus wood evaporator under varying intensities of solar incidence. Under 1 sun, the surface temperature reached 44.7 °C, which was among the highest values reported in previously published solar evaporator studies. From 0.5 to 3 suns, the top surface temperature of the Janus wood substantially increased from 34.3 to 64.7 °C, while the bottom brine temperature remained relatively stable, only increasing from 24.6 °C to 29.0 °C under the same conditions. These results confirm the relatively high thermal insulation properties of the Janus wood evaporator.

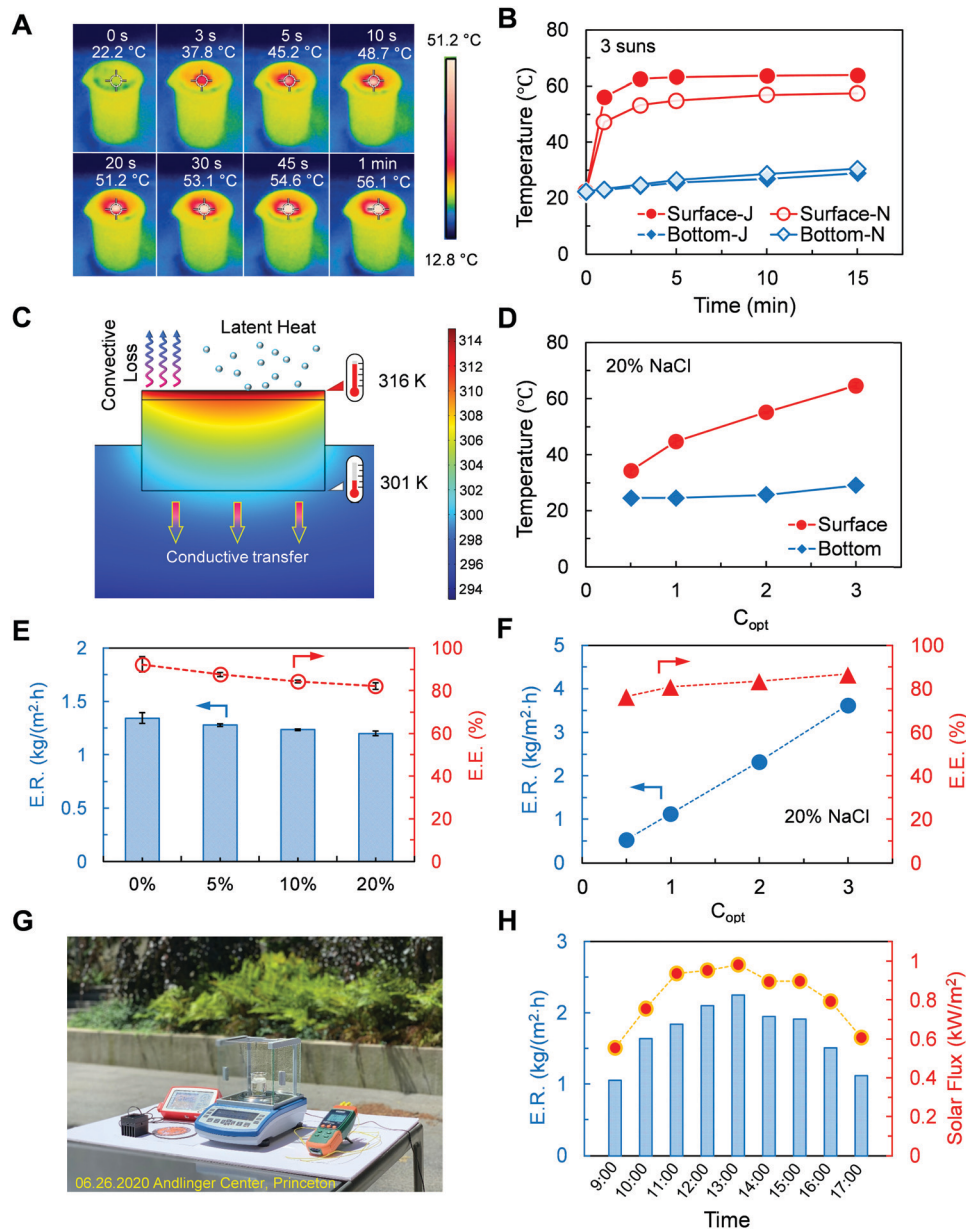


Fig. 3 High solar-thermal evaporation performance of a Janus wood evaporator in laboratory conditions and field tests. (A) Thermography images of the solar desalination module under 3 sun illumination with increasing time up to 60 s. (B) Time-dependent surface temperature changes of the Janus wood (J) and natural wood control (N) under 3 sun illumination. (C) Cross-sectional temperature profile of the Janus wood evaporator and the bulk brine under 1 sun incident illumination, modelled with COMSOL, indicating that the hydrophobic top layer improved heat insulation and localization. (D) Surface and bottom temperature changes of Janus wood at different optical concentrations. (E) The evaporation rate (E.R.) and evaporation efficiency (E.E.) of Janus wood at different salinities. (F) The E.R. and E.E. of Janus wood at different solar incidence concentrations. (G) Digital image of the solar-thermal evaporation module setup. (H) The hourly-average E.R. corresponding to the hourly-average natural solar flux.

Fig. 3E depicts the evaporation rate (E.R.) and evaporation efficiency (E.E.) of the Janus wood at different feed solution salinities (0%, 5%, 10%, and 20%) under 1 sun illumination. The E.R. slightly decreased from $1.35 \text{ kg m}^{-2} \text{ h}^{-1}$ to $1.20 \text{ kg m}^{-2} \text{ h}^{-1}$ as the salinity increased from 0% to 20%, while the E.E. gradually dropped from 92.3% to 82.0% (Fig. 3E). Such drops were expected as a higher salinity resulted in a lower vapor pressure, which can hinder evaporation.³⁹ Of note, the E.E. of 87.6% for 5% NaCl solution was the highest of all

published Janus thin-film evaporators (51–83.5%), even though most of them operated at a lower salinity of $\sim 3.5\%$ (Table S1, ESI†). Even at a high salinity of 20%, which has rarely been investigated, the Janus wood showed a very high E.E. of 82.0%. This efficiency was also much higher than those of wood-based evaporators used in other studies to distill feed solutions with lower salt concentrations (15% NaCl; E.E. of 57%).³⁵ Under larger solar fluxes, Janus wood achieved an even higher E.R. of $2.39 \text{ kg m}^{-2} \text{ h}^{-1}$ for 2 suns and $3.69 \text{ kg m}^{-2} \text{ h}^{-1}$ for 3 suns, with

corresponding E.E. values of 83.6% and 86.8%, respectively (Fig. 3F). Even for a lower optical concentration of 0.5 suns, which could be representative of the natural environment, the E.R. reached $0.59 \text{ kg m}^{-2} \text{ h}^{-1}$ with a good E.E. of 76.5%, indicating the viability of the Janus wood evaporator in real-world applications.

We also conducted field tests under natural conditions with varying solar flux and wind (Fig. 3G). The experiments were conducted from 9:00 to 17:00 in June in Princeton, New Jersey, using a 20% NaCl solution. The relative humidity was 50–60% and the ambient temperature was 26–35 °C. Fig. 3H shows a strong correlation between the hourly average E.R. and the solar flux. At the maximum solar flux of 0.98 kW m^{-2} , the highest E.R. was $2.25 \text{ kg m}^{-2} \text{ h}^{-1}$. The E.E. ranged from 131% to 167% during the field test, which indicates that natural wind considerably accelerated evaporation on top of the solar-thermal driving force. The field tests proved that the Janus

wood evaporator was able to maintain its desalination performance under naturally varying solar incidence, which indicates its promising potential in real-world applications.

System longevity and persistent salt-resistance

System longevity was tested by operating the Janus wood evaporator alongside the natural wood evaporator for ten consecutive cycles. For each cycle, the evaporator was operated continuously for 8 h under 1 sun, followed by 16 h in the dark to simulate natural daylight cycling. Fig. 4A shows the surface of the natural wood control over the course of the ten cycles. At the beginning of the test, the surface of the natural wood was easily wetted, and salt started to accumulate after the 1st cycle, almost covering the entire surface of the natural wood. By the end of the 10th cycle, a thick salt shell formed across the whole evaporator (Fig. 4A). In contrast, the surface of the Janus wood evaporator was dry and clean at the beginning. After the

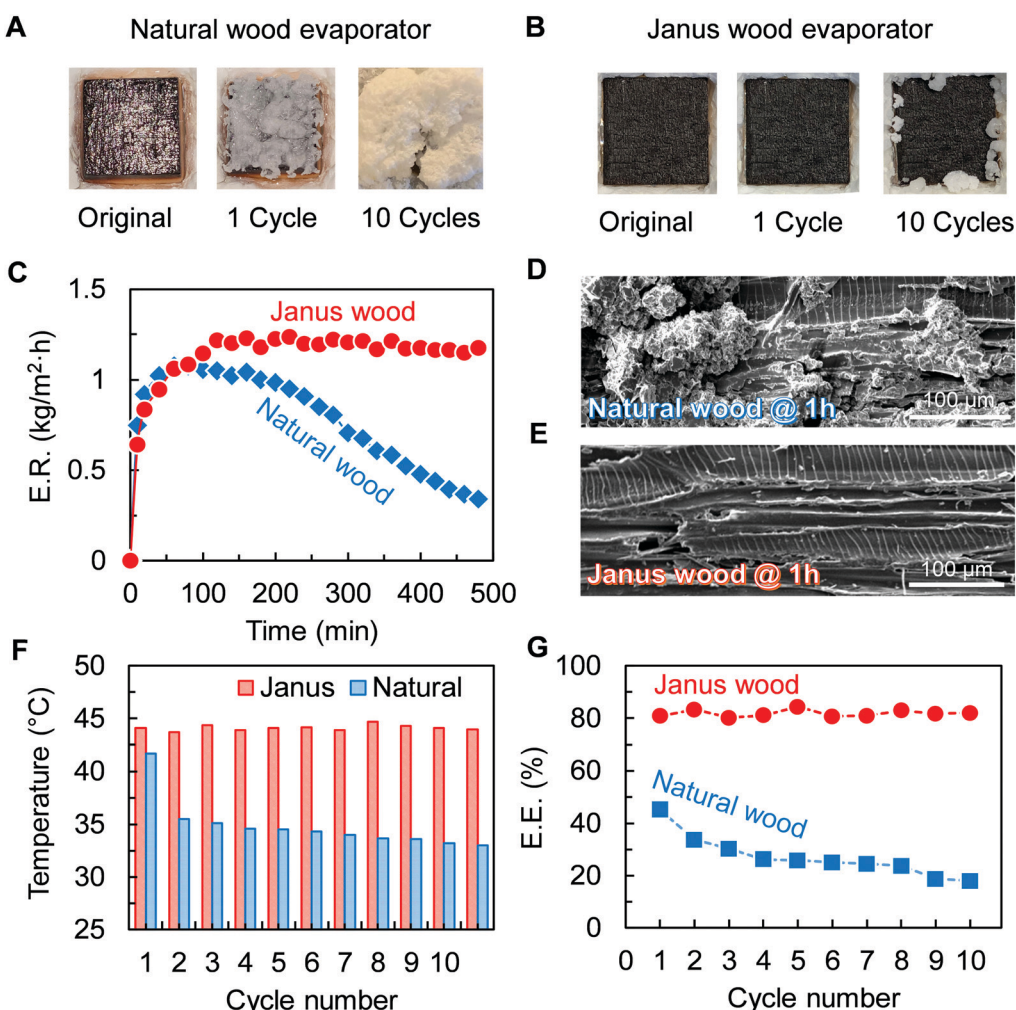


Fig. 4 Longevity tests of the Janus wood and natural wood. (A) Digital images of the natural wood evaporator before cycling experiments, after the 1st cycle, and after the 10th cycle. (B) Digital images of the Janus wood evaporator before cycling experiments, after the 1st cycle, and after the 10th cycle. (C) The evaporation rate (E.R.) of the wood evaporators during the 1st cycle. (D) SEM image of the top surface of the natural wood evaporator after operating for 1 h in the 1st cycle. (E) SEM image of the top surface of the Janus wood after operating for 1 h in the 1st cycle. (F) The surface temperature of the Janus wood vs. natural wood in each of the 10 cycles. (G) The evaporation efficiency (E.E.) of the Janus wood and natural wood in each of the 10 cycles.

1st cycle, no salt accumulation was observed on the surface (Fig. 4B), and after the 10th cycle, the surface of Janus wood remained clean and dry, with only a small number of salt crystals on the evaporator edge. This is likely to be attributed to the leakage of feeding water through the gap between the evaporator and foam holder, not through the evaporator itself. The images clearly show improved salt rejection by the Janus wood evaporator due to its hydrophobicity.

Fig. 4C compares the E.R. of two wood evaporators during the 1st cycle. It can be seen that the E.R. of the natural wood evaporator quickly increased to $1.08 \text{ kg m}^{-2} \text{ h}^{-1}$ within 60 min, but soon started to decay and hit a low level of $0.40 \text{ kg m}^{-2} \text{ h}^{-1}$. The SEM image taken at 1 h clearly showed that salt crystallization blocked a significant area on the natural wood evaporator (Fig. 4D). Therefore, the 63% decrease in E.R. was believed to be primarily due to the salt accumulation on the surface, which scattered the solar incident and hindered the vapor transport. In comparison, the E.R. of the Janus wood evaporator quickly increased to $>1.20 \text{ kg m}^{-2} \text{ h}^{-1}$ after 120 min and then remained at the same level without decay for the whole 8 h cycle (Fig. 4C). As expected, the SEM investigation of Janus wood showed a very clean surface without salt accumulation, where the channeled surface structure of the Janus wood evaporator could be clearly observed (Fig. 4E). By the end of the cycle, the E.R. of Janus wood was nearly 3 times larger than that of the natural wood evaporator.

Similar differences were observed in the 10-day, 10-cycle longevity test. During this period, the surface temperature of the Janus wood remained at around 44°C , likely to be a result of the clean and dry surface, which enabled high-efficiency solar-heat conversion (Fig. 4F). However, the surface temperature of the natural wood decreased from 41.7°C at the beginning to 35.5°C at the end of the 1st cycle, which then further decreased to 33.0°C by the end of the 10th cycle.

The E.E. of the Janus wood evaporator remained very stable at $>80\%$ during the longevity test, while the E.E. of the natural

wood evaporator decreased from 45.2% during the 1st cycle to 18.0% during the 10th cycle, indicating a severe performance decline due to salt accumulation (Fig. 4G). This downward trend kept occurring despite the stabilization of the surface temperature after the 3rd cycle (Fig. 4F). This is likely to be due to the continuous salt accumulation that blocked the vapor escape pathway and raised the humidity at the surface, hindering evaporation. As a result, the E.E. of the Janus wood was 4.6 times larger than that of the natural wood evaporator at the end of the 10-day test. This proves that the Janus wood evaporator has much better longevity and stability than the natural wood evaporator, and therefore holds a great promise for practical solar-thermal desalination of hypersaline waters.

Life cycle assessment of the solar-thermal evaporation system

There exist few studies exploring the global warming potential (GWP) of ZLD technologies, and no studies that specifically consider the GWP of Janus evaporators or other passive desalination systems. Therefore, to evaluate the environmental impacts of the Janus wood evaporator and compare them with other similar technologies, we conducted a preliminary life cycle assessment (LCA) based on the ISO Standard 14040,⁴⁰ defaulting to lab- and pilot-scale data, except in the case of lab processes that can be easily scaled up to an industrial equivalent. The detailed background is presented in Note 3 (ESI†). The Janus wood evaporators in this study were compared to three other systems modeled in this paper: an aerogel Janus evaporator (AJE) operating with a solution of 12% NaCl,⁴¹ an electrospun Janus mat (EJM) operating with a solution of 20% NaCl,³³ and a simplified RO system powered by either photovoltaics (PV) or on-grid (OG) electricity.⁴² As the systems evaluated in this study do not exist in the ecoinvent v3.5 database, each system was built and compared side-by-side based on industry and literature data. A majority of the CO_2 equivalent (CO_{2e}) emissions from each Janus evaporator system were a result of the evaporator production, since the environmental impacts of

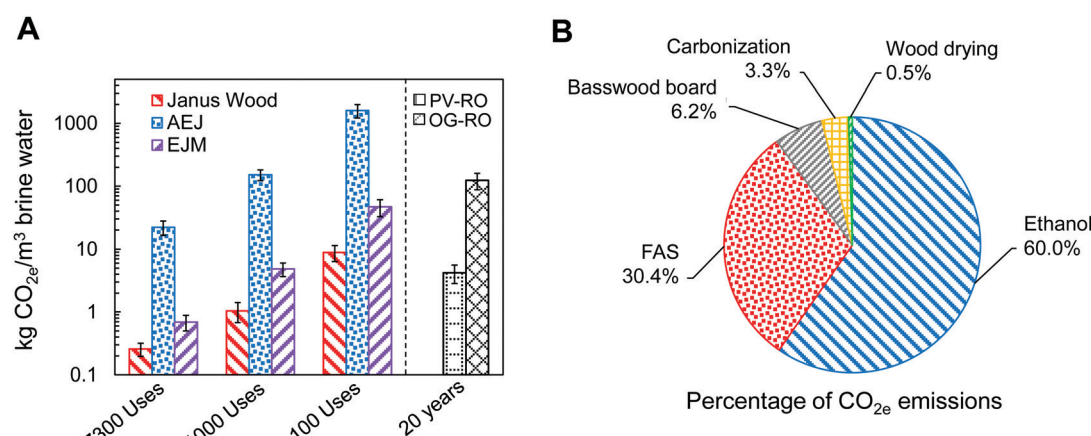


Fig. 5 Preliminary LCA of the Janus wood evaporator and three other systems. (A) The global warming potential of a Janus wood evaporator, an aerogel Janus evaporator (AJE), and an electrospun Janus mat (EJM), as it relates to the lifetime of each evaporator, as well as the global warming potential of photovoltaic (PV) and on-grid (OG) electricity-powered reverse osmosis (RO) systems. (B) The relative CO_{2e} emissions of each process or material involved in the production of Janus wood evaporators.

the tanks, photovoltaic panel, and pumps could span over a 20 years period (Fig. S12, ESI†).⁴³ A majority of the emissions from the systems featuring RO are a result of the high energy requirements in the pump operation that require energy from either the grid or very large photovoltaic panels (Fig. S13, ESI†).

Fig. 5 shows the results of the IPCC 2013 20a method for each system based on the number of uses of each evaporator before replacement. Janus wood outperformed the other Janus evaporators, emitting 2 orders of magnitude lower CO_{2e} than the AJE, and less than 20% of the CO_{2e} emissions of the EJM. However, with a shorter lifetime of each Janus wood evaporator, the GWP of the system greatly increases. Even though a Janus wood evaporator used less than 100 times is more sustainable than the OG–RO system, one that cannot be used more than 250 times is less sustainable than a PV–RO system with a lifetime of 20 years (Fig. 5A). However, the OG–RO and PV–RO systems likely undercount the real emissions due to its oversimplicity, and the GWP related to backwashing or membrane and PV-panel replacements was not considered. Therefore, it is likely that the required lifetime of a Janus wood evaporator would actually be significantly less. Further discussion on comparing the Janus wood evaporator with RO-based precipitation processes can be found in Note 5 (ESI†).

This result is promising for Janus wood as a more environmentally-friendly option for passive ZLD systems. While a significant majority of the environmental impact of the Janus wood evaporator system came from the evaporator itself, this process has not been optimized, which means that emissions can be further lowered in the future. For example, based upon a preliminary analysis of the GWP of each input in the Janus wood evaporator (Fig. 5B), the ethanol used during hydrophobization results in roughly 60% of the embodied CO_{2e} of the production of each evaporator, while the hydrophobic FAS (as modeled in this process) accounted for about 30% of the GWP of each evaporator. Focusing further research efforts toward the application of hydrophobic materials to carbonized wood would yield an even more environmentally-friendly hypersaline water desalination system.

Conclusion

In summary, a Janus wood evaporator with asymmetric wettability for highly efficient and stable desalination of hypersaline waters was engineered in a sustainable manner. With the enhanced heat localization, better heat insulation, and a higher surface temperature, the Janus wood evaporator achieved an impressive E.E. of 82.0% with 20% NaCl under 1 sun, which appeared to be the highest among the reported Janus evaporators operating under similar conditions. Moreover, the high salt-resistance led to very stable performance during long-term operation with an average evaporation efficiency of >80%, which was 4.6 times higher than the declining performance of a natural wood evaporator. The LCA demonstrated much lower CO_{2e} emissions in the Janus wood evaporator system *versus* other nanomaterial-based Janus evaporators. Further improvements

and more sustainable systems could also be a result of greener materials and fabrication processes, including choosing other materials like bamboo with a lower GWP, improving heating and carbonization techniques, optimizing the thicknesses of both the hydrophobic layer and bottom substrates, or exploring more environmentally-friendly hydrophobic chemicals. The Janus wood evaporator proposed in this study has great potential to solve water-based problems in a practical, sustainable, and energy-efficient way.

Materials and methods

Janus wood evaporator fabrication

The most suitable base wood substrate was selected from two common tree species, basswood and balsawood, each with two cutting directions, parallel and vertical to the growth direction (Fig. S3, ESI†). After comparative testing, the basswood cut parallelly to the growth direction demonstrated the best potential and was therefore chosen for preparing the Janus wood evaporator. A 1.5 × 1.5 × 1 cm³ wood block was tightly pressed on a 500 °C hot plate for 45 s to create a carbonized solar-thermal layer. This layer was then polished with a 2000 grit sandpaper and blown with compressed air to achieve a smooth and clean surface. The carbonized layer was about 1 mm in depth and had a black appearance. The carbonized solar absorber layer was then hydrophobized using a FAS solution, which contained the following (wt%): 2% FAS (perfluorodecyltrithoxysilane, C₁₆H₁₉F₁₇O₃Si; Sigma-Aldrich), 3% ultrapure water, and 95% ethanol. The pH of the solution was adjusted to 5.0 using acetic acid. This FAS solution was magnetically stirred for 24 h to ensure complete hydrolysis and evenly sprayed onto the carbonized side of the wood block. After the carbonized layer was completely covered by the FAS solution, the wood block was heated in a vacuum oven at 120 °C for 1 h at 80 kPa. The optical properties of the carbonized solar absorber surface kept unchanged after the hydrophobization treatment (Fig. S15, ESI†). The final hydrophobic layer of the Janus wood was ~1 mm thick (Fig. S16, ESI†), consistent with the depth of the carbonized layer, and had a FAS loading of 8.9 ± 0.7 mg cm⁻².

Material characterization

The contact angle was tested using a tensiometer (ramé-hart, Model 250) following a standard protocol. The morphology of wood evaporator samples was analyzed using scanning electron microscopy (FEI XL30 FEG-SEM). Thermography images were obtained using an infrared camera (FLIR, E5-XT). An ultra-violet-visible–near-infrared spectrophotometer (UV-vis, Lambda 35) equipped with an integrating sphere was used to detect the reflectance (*R*) and transmission spectra (*T*) of the solar absorber layer of the wood samples within 200–2500 nm, and the absorption (*A*) was calculated as *A* = 1 – *R* – *T*.

Solar-thermal evaporation experiment

The natural and Janus wood evaporators, with the carbonized sides facing up and away from the salt solution, were placed in

a synthetic saline water reservoir and exposed to simulated sunlight generated by a solar simulator with 300 W Xe-arc lamps (Newport, USA). Different concentrations of NaCl solution (0–20 wt%) were used in a suite of experiments with details explained in the results. The open area of the saline solution surface around the wood evaporator was covered by polyethylene foam to prevent direct evaporation from the reservoir. The whole system, including the wood evaporator, sealing foam, saline water, and the container, was placed on an electronic scale (B2, VWR, USA) with automated weight recording on a computer. A black curtain was used to separate the whole system from surrounding spaces, avoiding the impact of environmental wind or light on the evaporation process. The illumination intensity on the wood surface was tested using an optical power meter (THORLABS, USA) before and after each cycle.⁴⁴ A thermocouple (Siemens, Germany) was used to measure the temperature change of the wood surface and the bulk saline solution during the experiments. Data were recorded until the readings were stable. The evaporation efficiency of the system was calculated using eqn (1):

$$\eta = \dot{m} \cdot h_{\text{vap}} / (C_{\text{opt}} \cdot P_0) \quad (1)$$

where \dot{m} is the evaporation rate under illumination subtracted from the evaporation rate under dark conditions, h_{vap} is the total enthalpy associated with water evaporation, which includes the sensible heat and the enthalpy of phase change, C_{opt} is the solar incidence concentration, and P_0 is the nominal solar irradiation, 1 kW m⁻². The experiments were performed at room temperature (~23 °C) with a relative humidity of ~50%. All indoor experiments in this study were repeated at least three times and the error bars reflected standard deviations. Field tests were performed at Princeton, New Jersey, USA, with a 20% NaCl solution. The solar flux was measured every 10 min and averaged hourly. The relative humidity during the field test was 50–60% and the ambient temperature was 26–35 °C.

Modeling

COMSOL Multiphysics software was used to evaluate the temperature distribution across the wood evaporators and the feed water reservoir. The geometry of the wood evaporator was set based on the experimental measurements. Taking convective heat transfer to the ambient air and the internal convective/conductive heat transfer between the wood evaporator and feed water into consideration, the heat transfer in the semi-finite system can be expressed using eqn (2):

$$Q_{\text{In}} = \rho C_p \frac{\partial T(x, t)}{\partial t} + \rho C_p \mathbf{u} \cdot \nabla T(x, t) + \nabla [k \nabla T(x, t)] \quad (2)$$

where Q is the irradiative heat flux input; ρ , C_p , and k are the density, heat capacity, and thermal conductivity of the medium (*i.e.*, wood and water), respectively; $T(x, t)$ represents the local temperature at space vector x and time t ; and \mathbf{u} is the velocity field in the system, which was set to zero for simplification. An external irradiation source that provides constant heat flux of 1000 W m⁻² was set on top of the wood evaporator. The ambient air temperature was set to be 293 K. The relevant

parameter of water was loaded from material library built in COMSOL Multiphysics 5.5.

To simulate the latent heat for evaporation, we added a constant outward heat flux Q_{Evap} based on the experimentally acquired mass evaporation rate M using eqn (3):

$$Q_{\text{Evap}} = LM \quad (3)$$

where L is the specific latent heat of water. The convective heat transfer coefficient h was estimated using a simplified formula:

$$h = \frac{Ck_{\text{air}}}{W} \left(\frac{\rho^2 g \beta C_p \Delta T W^3}{\mu^2} \cdot \frac{\mu}{C_p k_{\text{air}}} \right)^n \quad (4)$$

where the constants C and n for a horizontal plate are 1.32 and 0.25, respectively; W is the width of the evaporator surface; k_{air} , ρ , β , μ and C_p are the thermal conductivity, density, thermal expansion coefficient, dynamic viscosity and heat capacity of air, respectively; and ΔT is the temperature difference between ambient air and the evaporative surface. The numerical simulations were conducted in the steady and transient analysis mode. Temperature distribution and heat transfer flux were obtained based on the simulation results.

Life cycle assessment

The Janus wood evaporators from this study were compared to three other systems modeled in this paper:

(1) An aerogel Janus evaporator (AJE) consisting of carbon nanotubes and cellulose nanofiber, with similar reported evaporation rate and testing conditions (~1.2 kg m⁻² at 1 sun and 12% NaCl).⁴¹ Note that the maximum NaCl concentration tested with the AJE was less than the concentration used in this study (20%). Therefore, it is likely that the results here undercount the actual emissions from that process.

(2) An electrospun Janus mat (EJM) composed of PMMA and PAN fibers covered in carbon black nanoparticles, operating in 20% NaCl and under the same conditions as those applied for the Janus wood.³³ Note that the EJM consisted of a thick foam and wick, which was not modeled in this analysis due to a lack of material details provided in the initial study. Therefore, it is likely that the results here undercount the actual emissions from that process.

(3) A simplified RO system powered by either photovoltaics (PV) or on-grid (OG) energy, based on Jijakli *et al.*, modeled in this work.⁴²

Goal and scope definition. The objective of this study was to compare the GWP of the Janus wood evaporator with that of three other systems of interest, primarily from the production phase and use phase of each system. Construction, digging, and brine and waste disposal were not in the scope of this analysis. The functional unit is 1 m³ of highly saline solution (20 wt% NaCl) treated per day over a 20 years system lifetime, where the final goal was ZLD each day. Other assumptions, including evaporator efficacy, hours of sunlight, and specific sun power at the evaporator surface, can be found in Table S2 (ESI†). Life-cycle assessment (LCA) of the designed evaporators was used to calculate the GWP, while ecoinvent v3.5 and openLCA 10.1.3 were utilized to quantify these impacts.

Inventory analysis. The life cycle inventory for each system included a polyvinylchloride tank, pumps to pump brine into the tank, photovoltaic cells to power the pumps, pipes, and anti-scalants and anti-foulants,⁴² each of which lasted for a total of 20 years. In the LCA models, each evaporator was used 100, 1000, or 7300 times (days) under the assumption that each would eventually become saturated by salt deposits, lose efficacy, and need to be replaced by a virgin evaporator. The inventories for each evaporator, including assumptions and calculation derivations, are included in Tables S5–S8 (ESI†). Note that most LCA data related to individual unit processes were taken from the ecoinvent 3.5 database, unless otherwise stated.

Impact assessment. The environmental impact of each evaporator system was determined using the 20a IPCC 2013 method, which measures the 20 years greenhouse gas emissions (CO₂ equivalent, CO_{2e}) per functional unit. This approach was also used for each of the use phase conditions (100 uses, 1000 uses, and 7300 uses).

Author contributions

X. C., Z. J. R., and L. H. contributed to the initial idea and experimental design. X. C., S. H., T. L., and D. S. conducted materials preparation and characterization. S. Z. carried out the COMSOL simulation. M. M. F. and Y. W. performed the life cycle assessment. X. C., J. D., Y. B., X. Z., and J. J. contributed to experimental analysis and schematics design. X. C., M. M. F., Z. J. R., and L. H. wrote the paper, and all authors commented on the final manuscript.

Conflicts of interest

The authors declare that they have no competing interests.

Acknowledgements

The authors acknowledge the use of Princeton's Imaging and Analysis Center, which is partially supported through the Princeton Center for Complex Materials (PCCM) and a National Science Foundation (NSF)-MRSEC program (DMR-2011750). We appreciate the financial support from the Princeton Catalysis Initiative (PCI) and the Materials Research Science and Engineering Center (MRSEC; DMR-1420541), National Science Foundation (NSF).

References

- (United Nations World Water Assessment Programme) WWAP, Leaving no one behind, 2019.
- Z. Wang, T. Horseman, A. P. Straub, N. Y. Yip, D. Li, M. Elimelech and S. Lin, *Sci. Adv.*, 2019, **5**, eaax0763.
- L. Zhang, Z. Xu, L. Zhao, B. Bhatia, Y. Zhong, S. Gong and E. N. Wang, *Energy Environ. Sci.*, 2021, **14**, 1771–1793.
- E. Jones, M. Qadir, M. T. H. van Vliet, V. Smakhtin and S. Mu Kang, *Sci. Total Environ.*, 2019, **657**, 1343–1356.
- M. Elimelech and W. A. Phillip, *Science*, 2011, **333**, 712–717.
- P. D. Dongare, A. Alabastri, O. Neumann, P. Nordlander and N. J. Halas, *Proc. Natl. Acad. Sci. U. S. A.*, 2019, **116**, 13182–13187.
- K. Zuo, W. Wang, A. Deshmukh, S. Jia, H. Guo, R. Xin, M. Elimelech, P. M. Ajayan, J. Lou and Q. Li, *Nat. Nanotechnol.*, 2020, **15**, 1025–1032.
- K. P. Lee, T. C. Arnot and D. Mattia, *J. Membr. Sci.*, 2011, **370**(1–2), 1–22.
- T. Tong and M. Elimelech, *Environ. Sci. Technol.*, 2016, **50**(13), 6846–6855.
- A. V. Dudchenko, C. Chen, A. Cardenas, J. Rolf and D. Jassby, *Nat. Nanotechnol.*, 2017, **12**, 557–563.
- E. J. Okampo and N. Nwulu, *Renewable Sustainable Energy Rev.*, 2021, **140**, 110712.
- S. Galliano, F. Bella, M. Bonomo, G. Viscardi, C. Gerbaldi, G. Boschloo and C. Barolo, *Nanomaterials*, 2020, **10**, 1–19.
- L. Fagiolari, M. Bonomo, A. Cognetti, G. Meligrana, C. Gerbaldi, C. Barolo and F. Bella, *ChemSusChem*, 2020, **13**, 6562–6573.
- F. Zhao, Y. Guo, X. Zhou, W. Shi and G. Yu, *Nat. Rev. Mater.*, 2020, **5**, 388–401.
- C. Finnerty, L. Zhang, D. L. Sedlak, K. L. Nelson and B. Mi, *Environ. Sci. Technol.*, 2017, **51**(20), 11701–11709.
- C. Zhang, Y. Shi, L. Shi, H. Li, R. Li, S. Hong, S. Zhuo, T. Zhang and P. Wang, *Nat. Commun.*, 2012, **12**, 998.
- X. Zhou, F. Zhao, Y. Guo, B. Rosenberger and G. Yu, *Sci. Adv.*, 2019, **5**(6), eaaw5484.
- H. Ghasemi, G. Ni, A. M. Marconnet, J. Loomis, S. Yerci, N. Miljkovic and G. Chen, *Nat. Commun.*, 2014, **5**, 4449.
- L. Zhou, Y. Tan, D. Ji, B. Zhu, P. Zhang, J. Xu, Q. Gan, Z. Yu and J. Zhu, *Sci. Adv.*, 2016, **2**(4), e1501227.
- P. Tao, G. Ni, C. Song, W. Shang, J. Wu, J. Zhu, G. Chen and T. Deng, *Nat. Energy*, 2018, **3**, 1031–1041.
- R. Li, L. Zhang, L. Shi and P. Wang, *ACS Nano*, 2017, **11**(4), 3752–3759.
- F. Zhao, X. Zhou, Y. Shi, X. Qian, M. Alexander, X. Zhao, S. Mendez, R. Yang, L. Qu and G. Yu, *Nat. Nanotechnol.*, 2018, **13**, 489–495.
- G. Ni, G. Li, S. V. Boriskina, H. Li, W. Yang, T. J. Zhang and G. Chen, *Nat. Energy*, 2016, **1**, 16126.
- Y. Shi, R. Li, Y. Jin, S. Zhuo, L. Shi, J. Chang, S. Hong, K. C. Ng and P. Wang, *Joule*, 2019, **12**, 841–864.
- M. Gao, L. Zhu, C. K. Peh and G. W. Ho, *Energy Environ. Sci.*, 2019, **12**, 841–864.
- S. Cao, Q. Jiang, X. Wu, D. Ghim, H. Gholami Derami, P. I. Chou, Y. S. Jun and S. Singamaneni, *J. Mater. Chem. A*, 2019, **7**, 24059–24091.
- Y. Pang, J. Zhang, R. Ma, Z. Qu, E. Lee and T. Luo, *ACS Energy Lett.*, 2020, **5**(2), 437–456.
- X. Zhou, F. Zhao, Y. Guo, Y. Zhang and G. Yu, *Energy Environ. Sci.*, 2018, **11**, 1985–1992.
- W. Zhang, X. Chen, G. Zhang, J. Li, Q. Ji, C. Hu, Z. J. Ren, H. Liu and J. Qu, *J. Mater. Chem. A*, 2020, **8**, 12089–12096.

30 G. Ni, S. H. Zandavi, S. M. Javid, S. V. Boriskina, T. A. Cooper and G. Chen, *Energy Environ. Sci.*, 2018, **11**, 1510–1519.

31 Y. Xia, Q. Hou, H. Jubaer, Y. Li, Y. Kang, S. Yuan, H. Liu, M. W. Woo, L. Zhang, L. Gao, H. Wang and X. Zhang, *Energy Environ. Sci.*, 2019, **12**, 1840–1847.

32 N. Xu, J. Li, Y. Wang, C. Fang, X. Li, Y. Wang, L. Zhou, B. Zhu, Z. Wu, S. Zhu and J. Zhu, *Sci. Adv.*, 2019, **5**(7), eaaw7013.

33 W. Xu, X. Hu, S. Zhuang, Y. Wang, X. Li, L. Zhou, S. Zhu and J. Zhu, *Adv. Energy Mater.*, 2018, **8**, 1702884.

34 Y. Yang, X. Yang, L. Fu, M. Zou, A. Cao, Y. P. Du, Q. Yuan and C. H. Yan, *ACS Energy Lett.*, 2018, **3**(5), 1165–1171.

35 S. He, C. Chen, Y. Kuang, R. Mi, Y. Liu, Y. Pei, W. Kong, W. Gan, H. Xie, E. Hitz, C. Jia, X. Chen, A. Gong, J. Liao, J. Li, Z. J. Ren, B. Yang, S. Das and L. Hu, *Energy Environ. Sci.*, 2019, **12**, 1558–1567.

36 J. Zhao, Y. Yang, C. Yang, Y. Tian, Y. Han, J. Liu, X. Yin and W. Que, *J. Mater. Chem. A*, 2018, **6**, 16196–16204.

37 X. Chen, X. Zhu, S. He, L. Hu and Z. J. Ren, *Adv. Mater.*, 2020, 2001240.

38 D. Hou, T. Li, X. Chen, S. He, J. Dai, S. A. Mofid, D. Hou, A. Iddya, D. Jassby, R. Yang, L. Hu and Z. J. Ren, *Sci. Adv.*, 2019, **5**(8), eaaw3203.

39 A. K. Menon, I. Haechler, S. Kaur, S. Lubner and R. S. Prasher, *Nat. Sustainable*, 2020, **3**, 144–151.

40 I. S. Arvanitoyannis, *Waste Management for the Food Industries*, 2008.

41 R. Hu, J. Zhang, Y. Kuang, K. Wang, X. Cai, Z. Fang, W. Huang, G. Chen and Z. Wang, *J. Mater. Chem. A*, 2019, **7**, 15333–15340.

42 K. Jijakli, H. Arafat, S. Kennedy, P. Mande and V. V. Theeyattuparampil, *Desalination*, 2012, **287**, 123–131.

43 Y. R. Pan, X. Wang, Z. J. Ren, C. Hu, J. Liu and D. Butler, *Environ. Int.*, 2019, **133**, 105266.

44 L. Lu, W. Vakki, J. A. Aguiar, C. Xiao, K. Hurst, M. Fairchild, X. Chen, F. Yang, J. Gu and Z. J. Ren, *Energy Environ. Sci.*, 2019, **12**, 1088–1099.